Monthly Notices
of the
ROYAL ASTRONOMICAL SOCIETY

MNRAS **489,** 5365–5380 (2019)
Advance Access publication 2019 September 07

doi:10.1093/mnras/stz2488

The presence of interstellar scintillation in the 15 GHz interday variability of 1158 OVRO-monitored blazars

J. Y. Koay,[1★] D. L. Jauncey,[2,3] T. Hovatta,[4,5] S. Kiehlmann,[6,7,8] H. E. Bignall,[9] W. Max-Moerbeck,[10] T. J. Pearson,[6] A. C. S. Readhead,[6] R. Reeves,[11] C. Reynolds[9] and H. Vedantham[12,13]

[1]*Institute of Astronomy and Astrophysics, Academia Sinica, Section 4, Roosevelt Rd., Taipei 10617, Taiwan*
[2]*CSIRO Astronomy and Space Science, Epping 1710, Australia*
[3]*Research School of Astronomy and Astrophysics, Australian National University, Canberra 2611, Australia*
[4]*Finnish Centre for Astronomy with ESO (FINCA), University of Turku, FI-20014 Turku, Finland*
[5]*Aalto University Metsähovi Radio Observatory, Metsähovintie 114, FI-02540 Kylmälä, Finland*
[6]*Owens Valley Radio Observatory, California Institute of Technology, Pasadena, CA 91125, USA*
[7]*Institute of Astrophysics, Foundation for Research and Technology-Hellas, GR-71110 Heraklion, Greece*
[8]*Department of Physics, University of Crete, GR-70013 Heraklion, Greece*
[9]*CSIRO Astronomy and Space Science, Kensington 6151, Australia*
[10]*Departamento de Astronomía, Universidad de Chile, Camino El Observatorio 1515, Las Condes, Santiago, Chile*
[11]*Departamento de Astronomía, Universidad de Conceptión, Concepción, Chile*
[12]*Cahill Center for Astronomy and Astrophysics, California Institute of Technology, 1200 E. California Blvd., Pasadena, CA 91125, USA*
[13]*Netherlands Institute for Radio Astronomy (ASTRON), Oude Hogeveensedijk 4, NL-7991 PD Dwingeloo, the Netherlands*

Accepted 2019 September 3. Received 2019 September 1; in original form 2019 July 12

ABSTRACT

We have conducted the first systematic search for interday variability in a large sample of extragalactic radio sources at 15 GHz. From the sample of 1158 radio-selected blazars monitored over an ∼10 yr span by the Owens Valley Radio Observatory 40-m telescope, we identified 20 sources exhibiting significant flux density variations on 4-d time-scales. The sky distribution of the variable sources is strongly dependent on the line-of-sight Galactic Hα intensities from the Wisconsin Hα Mapper Survey, demonstrating the contribution of interstellar scintillation (ISS) to their interday variability. 21 per cent of sources observed through sightlines with Hα intensities larger than 10 rayleighs exhibit significant ISS persistent over the ∼10 yr period. The fraction of scintillators is potentially larger when considering less significant variables missed by our selection criteria, due to ISS intermittency. This study demonstrates that ISS is still important at 15 GHz, particularly through strongly scattered sightlines of the Galaxy. Of the 20 most significant variables, 11 are observed through the Orion–Eridanus superbubble, photoionized by hot stars of the Orion OB1 association. The high-energy neutrino source TXS 0506+056 is observed through this region, so ISS must be considered in any interpretation of its short-term radio variability. J0616−1041 appears to exhibit large ∼20 per cent interday flux density variations, comparable in magnitude to that of the very rare class of extreme, intrahour scintillators that includes PKS0405−385, J1819+3845, and PKS1257−326; this needs to be confirmed by higher cadence follow-up observations.

Key words: scattering – ISM: general – galaxies: active – galaxies:jets – quasars: general – radio continuum: galaxies.

1 INTRODUCTION

The radio variability of compact active galactic nuclei (AGNs) provides a probe of extreme jet physics on scales comparable to or even exceeding that probed using VLBI techniques. Based on light-

★ E-mail: jykoay@asiaa.sinica.edu.tw

travel time arguments, variations observed on the shortest time-scales are expected to originate from the most compact regions, although this is complicated by the effects of relativistic beaming in blazars.

A further complication arises from interstellar scintillation (ISS; Heeschen & Rickett 1987; Rickett 1990; Jauncey et al. 2000), which has been shown to dominate blazar variability on time-scales of a few days or less at cm wavelengths. The 5 GHz Micro-Arcsecond Scintillation-Induced Variability (MASIV) Survey (Lovell et al. 2008) found that ∼60 per cent of 500 compact flat-spectrum AGNs monitored exhibit 2–10 per cent flux density variations on 2-d time-scales due to ISS. A follow-up survey (Koay et al. 2011a) also found ISS to dominate the intra and interday flux density variations at 8 GHz, as seen in other scintillation studies (e.g. Rickett, Lazio & Ghigo 2006).

While ISS has been observed in individual sources at 15 GHz (e.g. Savolainen & Kovalev 2008), there are no similar large-scale statistical studies of ISS at 15 GHz; variability at these frequencies is typically assumed to be predominantly intrinsic to the sources themselves.

The Owens Valley Radio Observatory (OVRO) blazar monitoring program (Richards et al. 2011) provides a rich data set for studying AGN variability at 15 GHz. It is the largest and most sensitive radio monitoring survey of blazars, and has been ongoing since the year 2008. The full sample of this OVRO monitoring program now comprises ∼1830 sources, each observed at a cadence of about twice a week, barring bad weather conditions and hardware issues.

The OVRO data have been used extensively to estimate the variability brightness temperatures of blazars (e.g. Liodakis et al. 2018a), study their radio–gamma-ray relationship (e.g. Max-Moerbeck et al. 2014; Richards et al. 2014) and perform multi-frequency cross-correlation studies of blazar flares (e.g. Hovatta et al. 2015; Liodakis et al. 2018b; Pushkarev et al. 2019). In these studies, the 15 GHz flux density variations are always assumed to be intrinsic to the blazar jets. Indeed the source variability amplitudes from the OVRO light curves, as quantified by the intrinsic modulation index (Richards et al. 2011), broadly show no significant Galactic dependence (Koay et al. 2018), confirming that intrinsic variations likely dominate. This is to be expected since this method of variability characterization is biased towards the largest inflections observed at the longest time-scales in the light curves, most of which are expected to be intrinsic to the blazars.

The only major studies of interstellar scattering using data from the OVRO monitoring program involved the sources J2025+3343 (Kara et al. 2012; Pushkarev et al. 2013) and J1415+1320 (Vedantham et al. 2017a). Symmetric U-shaped features observed in their light curves were attributed to or modelled as extreme scattering events (ESEs; Fiedler et al. 1987), arising from lensing by high-pressure intervening clouds of unknown origin in the interstellar medium. ESEs were subsequently ruled out as an explanation for J1415+1320 due to the achromatic behaviour of the U-shaped features up to mm-wavelengths (Vedantham et al. 2017a,b); the variations are instead ascribed to gravitational lensing by intervening structures.

Some questions remain – Is there significant variability in the OVRO blazar light curves on the shortest observed interday time-scales? If so, are these interday flux density variations intrinsic to the AGN or due to ISS? How prevalent is ISS at 15 GHz? Answering these questions is crucial for the interpretation of the OVRO light curves on the shortest observed time-scales, e.g. in multiwavelength studies of radio flares and jet physics like the ones referenced above. It is also important for the design of future surveys to study the radio variability of AGNs (and other compact sources) with next generation radio telescopes such as the Square Kilometre Array (Bignall et al. 2015) and its precursors (Murphy et al. 2013), where being able to distinguish between both forms of variability is needed to understand the underlying physics.

In this paper, we investigate the origin of the 15 GHz variability of the OVRO-monitored blazars on the shortest observed time-scale of ∼4 d. We use the term interday variability to define flux density variations occurring on a time-scale of days. This is the first ever study of interday variability at 15 GHz for such a large sample of sources. We describe the source sample briefly in Section 2, then characterize the 4-d variability amplitudes using the structure function in Section 3. In Section 4, we determine if ISS is responsible for the interday variability of these OVRO blazars by examining the Galactic dependence of their variability amplitudes, and discuss the implications of our results on blazar interday variability at 15 GHz. A summary of the paper is provided in Section 5.

2 SOURCE SAMPLE

For this study, we use the original sample of 1158 sources monitored by the OVRO 40-m telescope (Richards et al. 2011), selected from the Candidate Gamma-Ray Blazar Survey (CGRaBS; Healey et al. 2008). CGRaBS sources above a declination cut of $>-20^{\circ}$ were selected for monitoring by the OVRO telescope. The original CGRaBS sample was selected such that the sources would have spectral indices, radio flux densities, and X-ray flux densities similar to those of Energetic Gamma Ray Experiment Telescope (EGRET) detected sources, and would thus have a high chance of being detected in gamma-rays by *Fermi*. The CGRaBS sources were also selected to be outside $\pm10^{\circ}$ of the Galactic plane.

The OVRO telescope has been monitoring these sources at a cadence of around twice per week since 2008 to the present, subject to weather conditions and the instrument being operational. Additionally, about 20 per cent of the sources in the OVRO sample would be randomly selected each week to be observed only once that week, to fit into the schedule. Therefore, while the median time sampling of each source is about 4 d, the time lag between consecutive flux measurements in the OVRO light curves can be ∼8 d or more. For our analysis, we include flux density measurements up till 2018 April 10.

Richards et al. (2011) provide a detailed description of the observations and data reduction methodologies of the OVRO program.

3 CHARACTERIZATION OF VARIABILITY AMPLITUDES

3.1 The structure function

We use the structure function amplitude to characterize the strength of variability at different time-scales, given as:

$$D(\tau) = \frac{1}{N_\tau} \sum_{j,k} \left(\frac{S_j - S_k}{S_{15}} \right)^2, \quad (1)$$

where S_j and S_k represent a pair of measured flux densities separated by a time interval τ, binned to the nearest integer multiple of 4 d. S_{15} is the mean flux density calculated over the full light curve. N_τ is the number of pairs of flux densities in each time lag bin. We selected bins in integer multiples of $\tau = 4$ d since it is the typical smallest time lag between successive data samples in the OVRO

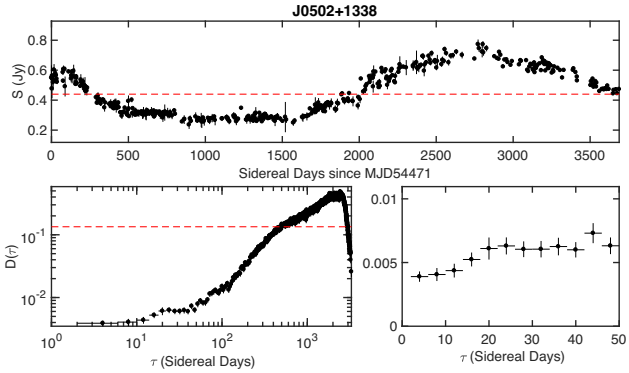

Figure 1. Top: Light curve for the source J0502+1338, where the horizontal dashed line denotes the mean flux density of the source. The error bars are given by equation (3) (Richards et al. 2011). Bottom: Structure function, $D(\tau)$, calculated from the light curve using equation (1), shown in its entirety in the left-hand panel, and for $\tau \leq 50$ d in the right-hand panel. The horizontal dashed line denotes D_{m15} (equation 2) derived from the intrinsic modulation indices estimated by Richards et al. (2014).

program for the majority of the sources. We note that N_τ typically decreases with increasing τ, with $N_{4\rm d} \approx 2N_{8\,\rm d}$, and so on. Bins were thus selected for plotting $D(\tau)$ and for our analysis only if $N_\tau \geq 30$. An example of a source light curve and the corresponding structure function is shown in Fig. 1 for the source J0502+1338. The error bars for $D(\tau)$ shown in the bottom panels of Fig. 1 are estimated as the standard error in the mean, defined as the ratio of the standard deviation of the $[(S_j - S_k)/S_{15}]^2$ terms in that particular time lag bin to $\sqrt{N_\tau - 1}$. This error estimate does not take into account the statistical errors due to the finite span of the OVRO observations, which would increase as τ increases relative to the total observing timespan.

As a sanity check, we compare $D(\tau)$ against the intrinsic modulation index, m_{15}, as determined using the maximum likelihood method by Richards et al. (2014). Since m_{15} is a measure of the standard deviation, whereas $D(\tau)$ is a measure of the variance, we convert m_{15} to an equivalent structure function amplitude following:

$$D_{m15} = 2(m_{15})^2 \ , \tag{2}$$

based on the assumption that the structure function amplitudes have saturated. Fig. 2 shows that $D(\tau)$ approaches and becomes comparable to D_{m15} as τ increases to the order of 100–1000 d. This confirms that m_{15} is more representative of the variability amplitude on time-scales of a hundred days or longer. We note that the $D(\tau)$ values shown here were derived from light curves in which outliers have been flagged (described in Section 3.2 below). Also, the m_{15} values derived by Richards et al. (2014) were based only on the first 4 yr of the OVRO data.

3.2 Data flagging and error estimation

Many of the OVRO light curves contain outliers that skew the structure function amplitudes. To automatically flag off these outliers, we first divided each source light curve into three contiguous segments of equal time period, then fit a sixth order polynomial to each segment. This segmentation enables better fits to the light curves, particularly those that exhibit rapid variations with many inflections over the full 10 yr period. We then remove data points for which the residuals are ≥4 times that of the rms residuals over

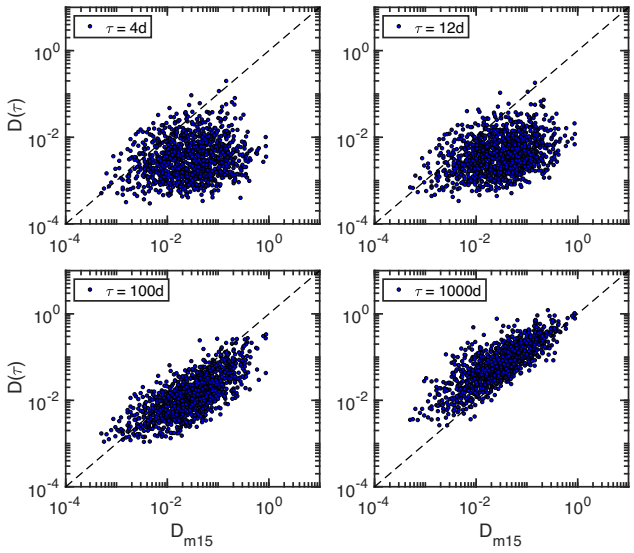

Figure 2. Structure function amplitudes, $D(\tau)$, for $\tau = 4$, 12, 100, 1000 d, plotted against D_{m15} derived using equation (2) from the intrinsic modulation indices, m_{15}, published by Richards et al. (2014). The dashed line shows the $x = y$ line.

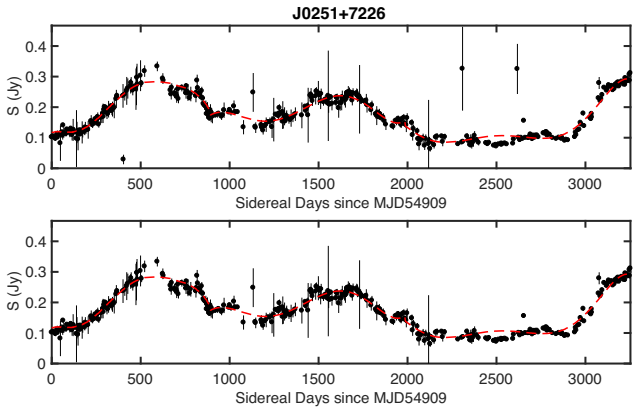

Figure 3. Example of automated flagging of the light curves for the source J0251+7226. Polynomial functions (dashed curves) are fit to three contiguous segments, then data points for which the fit residuals are ≥4 times the rms residuals are flagged. The top panel shows the light curve prior to flagging while the bottom panel shows the light curve after three outlier data points have been flagged automatically.

the corresponding segment. An example of this automatic flagging is shown in Fig. 3, for the source J0251+7226.

Errors in flux density measurements due to instrumental and other systematic effects contribute to the measured $D(\tau)$. One can be very conservative and assume that the flux density variations on the shortest measured time-scales, as characterized by $D(4\,\rm d)$, provides an upper limit on such errors in the flux density measurements. However, using $D(4\,\rm d)$ will overestimate the errors particularly in sources that exhibit real variability (whether ISS or intrinsic) on these short time-scales.

Since our goal is to examine if ISS is present in $D(4\,\rm d)$, we use instead the uncertainty of each single flux density measurement, described in Richards et al. (2011) and given by

$$\sigma_{\rm err} = \sqrt{\sigma_{15}^2 + (\epsilon \times S)^2 + (\eta \times \psi)^2}, \tag{3}$$

where σ_{15} is the scatter during each flux density measurement, and accounts for thermal noise, atmospheric fluctuations, and other stochastic errors. ϵ accounts for all the flux-dependent errors, including pointing and tracking errors. ψ is the switched power, and the η term accounts for systematic effects between the different beam switching pairs in each observation, caused by rapid atmospheric variations or pointing errors. The values of ϵ and η were determined from data of sources that show little or very slow variations, using the fitting methods described in Richards et al. (2011). These were checked for different observing epochs, and large changes were seen, for example, when the receiver was upgraded in 2014 May. The value of ϵ depends strongly on whether the source was used as a pointing source (with values ranging from 0.006–0.017) or if it was observed within 15° of a pointing source (classified as an 'ordinary source' with values between 0.014 and 0.036), with the former showing expectedly smaller pointing induced errors. The value of η is also seen to differ between pointing sources (values between 1.22 and 2.24) and ordinary sources (values between 0.47 and 1.59), showing that the switched power measurements also have a dependence on flux density, as the pointing sources are typically brighter than the ordinary sources.

As described in Richards et al. (2011), in some cases it is evident that the values of η and ϵ result in too large uncertainties for some objects, which clearly show common long-term trends with scatter about the mean smaller than expected from the error model. In order to account for this effect, a cubic spline fit was used to determine a scaling factor that is then applied to scale the uncertainty due to the flux density and switched power (see Richards et al. 2011, for details). This was not applied to the data taken after the receiver upgrade in 2014 May so that some of the uncertainties in the data may still be overestimated.

$\sigma_{\rm err}$ in equation (3) also does not include the uncertainty introduced by the flux density calibration, due to possible variability of the flux calibrator sources. This is typically assumed to be ~ 5 per cent based on the observed long-term variability of the flux calibrators, but is expected to be lower on interday time-scales. We estimate the flux calibration errors on 4-d time-scales to be ~ 1 per cent of the source mean flux density; the justification for this value is described in Appendix A.

For each source, we thus estimate the total contribution of noise, calibration, and other systematic errors to the observed 4-d modulation indices as the quadratic sum of the median value of $\sigma_{\rm err}$ and the ~ 1 per cent flux calibration errors, normalized by the mean flux density (see equation in Appendix A)

$$m_\sigma = \frac{\sqrt{(\mathrm{median}(\sigma_{\rm err}))^2 + (0.01 S_{15})^2}}{S_{15}}. \quad (4)$$

The rationale behind equation (4) is that the total error estimate determines how much the flux densities can vary from one measurement to the next, in the absence of real astrophysical variability; m_σ thus represents the estimated error contribution to the variability amplitudes on the shortest observed time-scales. We use the median instead of the mean $\sigma_{\rm err}$ value, since the presence of a few large $\sigma_{\rm err}$ in a light curve (as can be seen in Figs 1 and 3) skews the mean towards larger values, which in turn may overestimate the errors. As a check, when we use the mean instead of the median $\sigma_{\rm err}$ value to estimate m_σ, we find that the distribution of $m_{D(4\,\mathrm{d})}/m_\sigma$ peaks at values <1, where $m_{D(4\mathrm{d})}$ is the modulation index derived from $D(4\,\mathrm{d})$ using equation (2); this suggests that using the mean of $\sigma_{\rm err}$ overestimates m_σ for each source.

A diagnostic plot of $m_{D(4\,\mathrm{d})}$ (in red) versus 15 GHz mean flux density is shown in Fig. 4. Overlayed are plots of m_σ (in blue) for each source. The dashed line shows the following fit to m_σ:

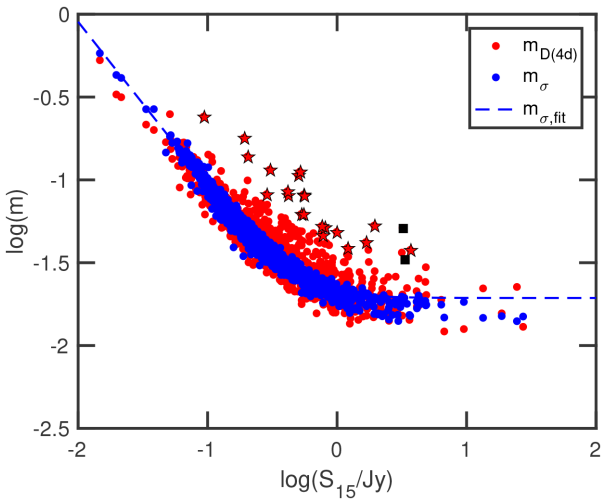

Figure 4. Modulation indices derived from the 4-d structure function amplitude, $m_{D(4\,\mathrm{d})}$, and the total contribution of instrumental, calibration, and other systematic errors to the observed 4-d modulation indices of each source, m_σ, plotted against the mean 15 GHz flux density. The red star symbols denote sources for which $m_{D(4\,\mathrm{d})} \geq 2m_\sigma$. The dashed line denotes the best fit of equation (5) to m_σ. The black squares show $m_{D(4\,\mathrm{d})}$ for two blazars observed through the Galatic plane that were not included in our sample but were also monitored by OVRO since 2008, i.e. 3EGJ 2016+3657 and 3EGJ 2027+3429 (see Section 4.3).

$$m_{\sigma,\mathrm{fit}} = \sqrt{p^2 + (s/S_{15})^2}, \quad (5)$$

where s collates all the flux independent errors, i.e. σ_{15} and $\eta \times \psi$ in equation (3), while p collates all the flux dependent errors. We obtained best-fitting values of $p = 0.0194$ and $s = 0.009$ Jy for m_σ.

From Fig. 4, we see that $m_{D(4\,\mathrm{d})}$ is generally comparable to m_σ for the large majority of sources, displaying a similar flux density dependence. This is to be expected if $m_{D(4\,\mathrm{d})}$ is dominated by noise and systematic uncertainties as characterized by equation (5) for the majority of sources. This is also demonstrated in Fig. 5 where the distribution of $m_{D(4\,\mathrm{d})}/m_\sigma$ peaks at a value of $\sim$1, for both the $S_{15} \geq 0.8$ and $S_{15} < 0.8$ Jy sources. As shown in Fig. A1 and discussed in Appendix A, not including the estimated 1 per cent flux calibration errors results in an underestimation of m_σ for the $S_{15} \geq 0.8$ Jy. The tail towards larger values of $m_{D(4\mathrm{d})}/m_\sigma$ (>1.5) suggests the presence of real astrophysical variability in a fraction of the OVRO sources at these 4-d time-scales; 21 of the 1158 sources (1.8 per cent) show 4-d variability amplitudes $\geq$2 times that of m_σ. We discuss the origin of this variability in the next section.

4 RESULTS AND DISCUSSION

4.1 Galactic dependence of variability amplitudes

For our full sample of 1158 sources, we now examine if their variability amplitudes on time-scales of days and weeks show a Galactic dependence, which would provide strong evidence for the presence of ISS. The top panel of Fig. 6 shows $D(4\,\mathrm{d})$ plotted against the line-of-sight Hα intensities (I_α) obtained from the Wisconsin H-Alpha Mapper (WHAM) Survey (Haffner et al. 2003). Since the Hα intensities are a measure of the integral of the squared electron densities along the line of sight, they provide a proxy for the line-of-sight interstellar scattering strength. Indeed, the intra and interday

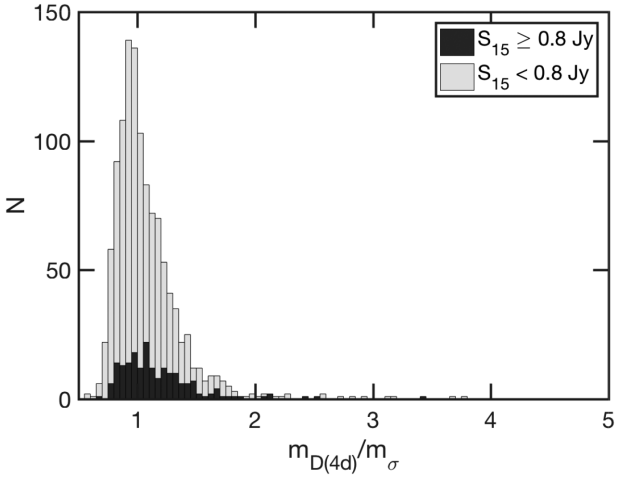

Figure 5. Histogram showing the distribution of the ratio of the 4-d variability amplitudes to the flux normalized measurement uncertainties of each source, $m_{D(4\,d)}/m_\sigma$. The histograms peak at a value of ∼1 for both the $S_{15} \geq 0.8$ and $S_{15} < 0.8$ Jy sources, when the 1 per cent flux calibration errors are included. The errors in the $S_{15} \geq 0.8$ Jy sources are likely underestimated when excluding the flux calibration errors (Appendix A).

variability amplitudes of blazars at 2 GHz (Rickett et al. 2006), 5 GHz (Lovell et al. 2008), and 8 GHz (Koay et al. 2012) show significant correlations with line-of-sight Galactic H α intensities, demonstrating that their flux density variations are dominated by ISS.

For both the weak and strong source samples, there is a clear excess of sources with larger amplitude variability for sightlines where $I_\alpha \geq 10$ Rayleighs (R). Spearman correlation tests show a statistically significant relationship between $D(4\,d)$ and the line-of-sight H α intensities (p-value of 2.67×10^{-4}), as shown in Table 1. We have chosen a significance level of $\alpha = 0.05$. This H α dependence of the 15 GHz variability amplitudes demonstrates the presence of ISS in the OVRO light curves, at least in sources observed through heavily scattered lines of sight. In fact, this correlation between $D(\tau)$ and I_α remains statistically significant up to a time-scale of $\tau \sim 80$ d (Table 1). However, on time-scales of 100 d and above, this correlation is no longer significant as intrinsic variations likely begin to dominate.

The Spearman correlation tests may be biased by the extreme $I_\alpha \geq 10$ R sources. We therefore repeat the same tests using only sources with line of sight $I_\alpha < 10$ R. We find that the correlation between $D(\tau)$ and I_α remains significant, up to a time-scale of ∼20 d. This suggests that at 15 GHz, while the variability of sources seen through heavily scattered sightlines ($I_\alpha \geq 10$ R) may be dominated by ISS up to time-scales of 80 d, ISS is significant up to only ∼20 d time-scales for more typical sightlines through the Galaxy where $I_\alpha < 10$ R.

As further confirmation, we examine in Fig. 7 the distribution of $D(4\,d)$ for sources with low ($I_\alpha < 1$ R, top), moderate ($1\,R \leq I_\alpha < 10$ R, middle), and high ($I_\alpha \geq 10$ R, bottom) line-of-sight H α intensities. The Kolmogorov–Smirnov (K–S) test confirms that the distribution of $D(4\,d)$ for sources with high I_α is significantly different from that of the combined sample of sources with low and moderate I_α, at a p-value of 6.45×10^{-6}. The mean value of $D(4\,d)$ for sources with $I_\alpha \geq 10$ R is 0.0143, a factor of ∼2 higher than the value of 0.0061 for that of sources with $I_\alpha < 10$ R.

Although we see no obvious correspondence between $D(4\,d)$ and the Galactic latitudes by eye (Fig. 6, bottom), the Spearman

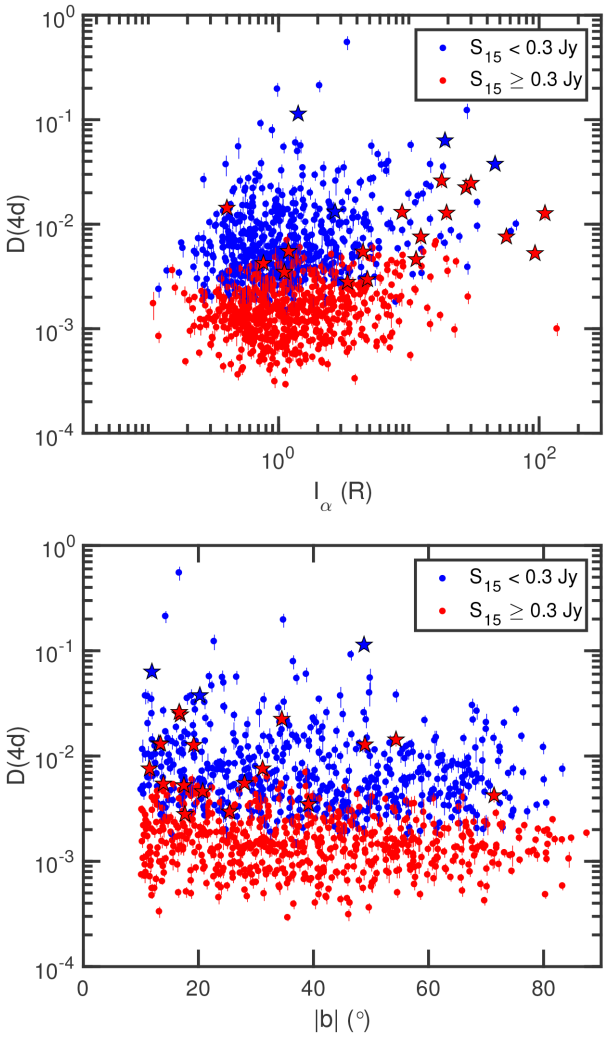

Figure 6. Structure function amplitude at 4-d time-scales, $D(4\,d)$, versus line-of-sight H α intensity (top) and Galactic latitude (bottom). The sources are separated into two roughly equal samples of high flux density ($S_{15} \geq 0.3$ Jy, red) and low flux density ($S_{15} < 0.3$ Jy, blue) sources. The star symbols denote the most significant variables in our sample (discussed in Section 4.2). The fact that the relationship between $D(4\,d)$ and I_α is evident for both the weak and strong source samples confirms that this relationship is not due the presence of noise in the $D(4\,d)$ of the weaker sources.

correlation test reveals a statistically significant anticorrelation between $D(\tau)$ and $|b|$ on time-scales of 4–20 d (Table 1). The correlation coefficients are weaker compared to that between $D(4\,d)$ and I_α. The H α intensities are therefore a better indicator of line-of-sight scattering strength compared to the Galactic latitudes, due to the complex structure of the ionized gas in the Galaxy. This is in spite of the 1° angular resolution of the WHAM Survey data.

4.2 ISS of the most significant interday variables

Since $D(4\,d)$ still comprises significant amounts of instrumental and systematic errors in a large fraction of sources (i.e. the peak of $m_{D(4\,d)}/m_\sigma$ is close to unity), we now examine only the most significant variables at 4-d time-scales to determine the origin of their variability. We consider sources satisfying the criteria that $m_{D(4\,d)} \geq 2m_\sigma$ to be significantly variable, based on the tail end of the $m_{D(4\,d)}/m_\sigma$ distribution in Fig. 5. We initially find 21

Table 1. Spearman rank correlation coeffficients, r_s, and corresponding p-values between pairs of parameters and for various source samples.

Parameter 1	Parameter 2	Source sample	No. of sources	r_s	p-value	Significant? ($\alpha = 0.05$)
D(4 d)	I_α	All	1158	0.107	2.67×10^{-4}	Y
D(8 d)	I_α	All	1158	0.111	1.47×10^{-4}	Y
D(12 d)	I_α	All	1158	0.121	3.54×10^{-5}	Y
D(16 d)	I_α	All	1158	0.118	5.97×10^{-5}	Y
D(20 d)	I_α	All	1158	0.112	1.35×10^{-4}	Y
D(40 d)	I_α	All	1158	0.073	1.26×10^{-2}	Y
D(60 d)	I_α	All	1158	0.068	2.03×10^{-2}	Y
D(80 d)	I_α	All	1158	0.063	3.17×10^{-2}	Y
D(100 d)	I_α	All	1158	−0.055	5.95×10^{-2}	N
D(1000 d)	I_α	All	1158	−0.047	1.12×10^{-1}	N
D(4 d)	I_α	$I_\alpha < 10$	1104	0.059	4.87×10^{-2}	Y
D(8 d)	I_α	$I_\alpha < 10$	1104	0.065	3.18×10^{-2}	Y
D(12 d)	I_α	$I_\alpha < 10$	1104	0.082	6.30×10^{-3}	Y
D(16 d)	I_α	$I_\alpha < 10$	1104	0.078	9.20×10^{-3}	Y
D(20 d)	I_α	$I_\alpha < 10$	1104	0.077	1.04×10^{-2}	Y
D(40 d)	I_α	$I_\alpha < 10$	1104	0.041	1.74×10^{-1}	N
D(60 d)	I_α	$I_\alpha < 10$	1104	0.036	2.39×10^{-1}	N
D(80 d)	I_α	$I_\alpha < 10$	1104	0.032	2.85×10^{-1}	N
D(100 d)	I_α	$I_\alpha < 10$	1104	−0.029	3.44×10^{-1}	N
D(1000 d)	I_α	$I_\alpha < 10$	1104	−0.018	5.42×10^{-1}	N
D(4 d)	$\|b\|°$	All	1158	−0.072	1.40×10^{-2}	Y
D(8 d)	$\|b\|°$	All	1158	−0.075	1.04×10^{-2}	Y
D(12 d)	$\|b\|°$	All	1158	−0.090	2.30×10^{-3}	Y
D(16 d)	$\|b\|°$	All	1158	−0.086	3.50×10^{-3}	Y
D(20 d)	$\|b\|°$	All	1158	−0.084	4.40×10^{-3}	Y
D(40 d)	$\|b\|°$	All	1158	−0.045	1.25×10^{-1}	N
D(60 d)	$\|b\|°$	All	1158	−0.038	1.94×10^{-1}	N
D(80 d)	$\|b\|°$	All	1158	−0.033	2.61×10^{-1}	N
D(100 d)	$\|b\|°$	All	1158	−0.026	3.75×10^{-1}	N
D(1000 d)	$\|b\|°$	All	1158	−0.217	4.75×10^{-1}	N

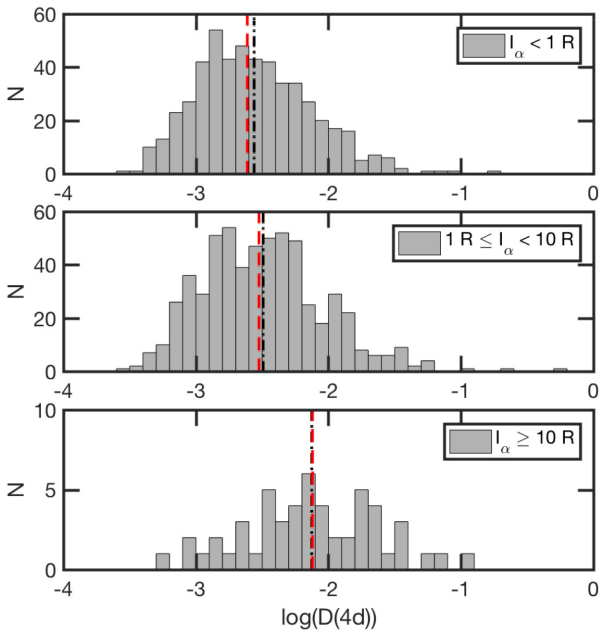

Figure 7. Histograms showing the distributions of D(4 d) for sources with low ($I_\alpha < 1$ R, top), moderate (1 R $\leq I_\alpha <$ 10 R, middle), and high ($I_\alpha \geq$ 10 R, bottom) line-of-sight Hα intensities. The dashed (red) and dash–dotted (black) vertical lines show the median and mean values of D(4 d), respectively. The $I_\alpha \geq$ 10 R sample of sources contain a significantly higher fraction of interday variables.

significant interday variables that meet these criteria. After careful inspection (described in Appendix B), we found that the light curve of J0259−0018, the weakest (∼0.1 Jy) and most variable ($m_{D(4\,\mathrm{d})} \sim$ 24 per cent) of these 21 sources, was severely affected by an error in source coordinates in the OVRO and CGRaBS catalogues. We therefore remove it from our sample of significant interday variables and refer to the remaining 20 sources as 'interday variables' for the rest of this paper. The full list of these interday variables is shown in Table 2, together with their variability amplitudes. Their light curves are presented in Appendix C.

The flux density variations of these interday variables are clearly dominated by ISS, as evidenced by the larger fraction of variables detected among sources with larger I_α values. 11 (21 per cent) of the 53 sources with line-of-sight $I_\alpha \geq$ 10 R are classified as interday variables, while only ∼ 0.8 per cent (9/1104) of sources with $I_\alpha <$ 10 R are classified as such.

ISS arises due to the scattering of radio waves by density inhomogeneities of the free electrons in the ionized interstellar medium. This scattering process is often well-described as being confined to a single thin scattering screen located between the source and the observer; this screen changes the phases of an incoming plane wave (Narayan 1992). Compact AGN are known to exhibit ISS in two different regimes (Rickett 1990; Narayan 1992), weak ISS and strong refractive ISS (Blandford, Narayan & Romani 1986; Rickett 1986; Coles et al. 1987). In the weak ISS regime, phase changes in the wavefront due to diffractive scattering are less than a radian, so that the scintillation pattern is dominated by the Fresnel scale, $r_\mathrm{F} = \sqrt{c D_\mathrm{L}/(2\pi\nu)}$, where c is the speed of light, D_L is the distance from the observer to the scattering

Table 2. List of the interday variables and their mean flux densities, variability amplitudes, and line-of-sight H α intensities.

Name (J2000)	S_{15} (Jy)	D_{4d}	$m_{D(4\,d)}$	m_σ	$m_{D(4\,d)}/m_\sigma$	l (°)	b (°)	I_α (R)
J0050−0929	0.781	4.22e−03	0.046	0.020	2.29	122.35	−71.39	0.77
J0128+4901	0.556	1.30e−02	0.081	0.027	3.02	129.10	−13.41	8.88
J0238+1636	1.689	3.48e−03	0.042	0.014	2.95	156.77	−39.11	1.11
J0336−1302	0.422	1.28e−02	0.080	0.030	2.71	201.14	−48.94	19.49
J0401+0413	0.505	2.25e−02	0.106	0.027	3.92	186.03	−34.49	27.49
J0407+0742	0.534	7.59e−03	0.062	0.025	2.47	183.87	−31.16	12.37
J0449+1121	1.001	4.61e−03	0.048	0.021	2.28	187.43	−20.74	11.37
J0527+0331	0.522	2.47e−02	0.111	0.028	3.99	199.79	−16.85	29.99
J0529−0519	0.206	3.77e−02	0.137	0.053	2.61	207.68	−20.25	45.94
J0541−0541	0.811	5.26e−03	0.051	0.022	2.32	208.75	−17.48	93.06
J0542−0913	0.561	1.27e−02	0.080	0.025	3.15	213.12	−19.18	110.97
J0552+0313	0.554	7.59e−03	0.062	0.026	2.41	203.23	−11.48	56.16
J0610−1847	0.306	2.61e−02	0.114	0.035	3.28	224.10	−16.66	17.87
J0616−1041	0.193	6.32e−02	0.178	0.055	3.21	217.39	−11.91	18.94
J0721+7120	1.959	5.52e−03	0.053	0.012	4.51	143.98	28.02	1.19
J0725+1425	0.768	5.45e−03	0.052	0.021	2.49	203.64	13.91	4.45
J0824−1527	0.288	1.32e−02	0.081	0.036	2.28	237.08	13.12	2.71
J1135−0428	0.417	1.43e−02	0.085	0.030	2.85	269.31	54.34	0.40
J1642−0621	1.216	2.96e−03	0.038	0.015	2.52	11.48	25.41	4.82
J1751+0939	3.717	2.80e−03	0.037	0.011	3.37	34.92	17.65	3.38

Note: (2) 15 GHz mean flux density; (3) 4-d structure function amplitude; (4) modulation index derived from $D(4\,d)$ using equation (2); (5) uncertainties in flux measurements, representing the contribution of instrumental and non-astrophysical effects to the measured variability amplitudes; (6) significance of 4-d variability amplitude, as defined by the ratio of the 4-d modulation index to the uncertainties in flux measurements; (7–8) Galactic coordinates; (9) line-of-sight H α intensity (Haffner et al. 2003).

screen, and ν is the observing frequency. In other words, weak ISS is observed at frequencies and sightlines where the diffractive length-scale, $r_{\rm diff}$, is much larger than $r_{\rm F}$. On the other hand, the focussing and defocussing of coherent patches of waves due to the large-scale density fluctuations on the scattering screen lead to strong refractive ISS, observed when $r_{\rm diff} \ll r_{\rm F}$. ISS amplitudes are typically strongest at the transition frequency, ν_0, between weak and strong ISS (Narayan 1992). The modulation index of flux density variations scale as $(\nu_0/\nu)^{17/12}$ for weak ISS (observed at $\nu \gg \nu_0$) and scale as $(\nu/\nu_0)^{17/30}$ for strong refractive ISS (Walker 1998) observed at $\nu \ll \nu_0$. These assume a Kolmogorov power spectrum of turbulence (Goldreich & Sridhar 1995), as typically observed for the interstellar medium of the Milky Way (Armstrong, Rickett & Spangler 1995).

Analytical solutions for the spatial coherence function of flux densities, $\Gamma_4(r;\,\nu)$, measured at two locations on the Earth separated by a distance r, are provided by e.g. Coles et al. (1987) and Narayan (1992) for both the weak and strong ISS regimes. However, there are no analytical solutions for the intermediate scintillation regimes relevant for our study, where $\nu \approx \nu_0$. We therefore use the Goodman & Narayan (2006) fitting function derived from numerical simulations for calculations of $\Gamma_4(r;\,\nu)$ for our ensuing discussions, which is applicable at observing frequencies close to the transition frequency. By assuming that the density fluctuations on the scattering screen (and hence phase fluctuations imprinted on the scattered wave) are frozen and do not change on the time-scales of interest, we can estimate theoretical values of $D(4\,d) = 2[\Gamma_4(0;\,\nu) - \Gamma_4(r = v_s \times 4\,d;\,\nu)]$, where v_s is the relative transverse velocity between the scattering screen and the Earth.

At mid to high Galactic latitudes where ν_0 is typically 5–8 GHz (Walker 1998, 2001), a source must contain a compact component of angular size $\theta \sim$ 50–200 μas to scintillate at amplitudes of 2–10 per cent at 5 GHz, as observed in the MASIV Survey (Lovell et al. 2008). At similar lines of sight with comparable scattering strengths, we expect sources with the same range of angular sizes to exhibit weak ISS with modulation indices of 0.5–2 per cent at 15 GHz, as inferred from the Goodman & Narayan (2006) fitting function described above. We have assumed fiducial scattering screen distances of $D_{\rm L} = 500$ pc and transverse velocities of $v_s = 30\,{\rm km\,s^{-1}}$.

With the exception of 1 source exhibiting 18 per cent flux density variations, the other interday variables that we detect at 15 GHz exhibit 3–13 per cent flux density variations on 4-d time-scales, comparable to the typical ISS amplitudes observed at 5 GHz. This higher than expected 15 GHz ISS amplitudes can be explained if the interday variables are more compact (with $\theta \sim$ 5–40 μas) than the typical source observed in the MASIV Survey ($\theta \sim$ 50–200 μas) at 5 GHz. This is in excess of the source size–frequency relation of $\theta \propto \nu^{-1}$ expected for conical jets (Blandford & Königl 1979).

Therefore, if the interday variables from this study and the 5 GHz scintillators from the MASIV survey are drawn from the same underlying source populations, their source sizes must exhibit a frequency dependence of $\theta \propto \nu^{-k}$, where k is between 1.5 and 2. These values of k are in fact consistent with angular broadening due to scattering in the ISM, where the size of the scattering disc or scattered source image, $\theta_{\rm scatt}$, is expected to scale with frequency as $\theta_{\rm scatt} \propto \nu^{-2}$ (e.g. Rickett 1990). For example, scatter broadening at a second, more distant screen in the ISM can cause the apparent source size to increase more rapidly with decreasing frequency, compared to the frequency scaling of the intrinsic source size. This leads to the suppression of the scintillation amplitudes at 5 GHz relative to that at 15 GHz, as observed through the more nearby scattering screen primarily responsible for the ISS. This 2-screen scattering example is analogous to the suppression of solar-wind induced interplanetary scintillation of compact radio sources, when observed through sightlines with strong interstellar scattering (e.g. Duffett-Smith & Readhead 1976). Indeed, a previous study has shown that the frequency dependence of ISS amplitudes measured at 5 and 8 GHz simultaneously is consistent with a $\theta \propto \nu^{-2}$ relation for

sources observed through strongly scattered sightlines (Koay et al. 2012). This explanation is supported by the fact that the fraction of sources exhibiting significant 15 GHz ISS increases dramatically for sources observed through $I_\alpha \geq 10$ R compared to that with $I_\alpha < 10$ R.

Another simpler explanation for the relatively high-amplitude ISS at 15 GHz is that these interday variables are observed through sightlines where the transition frequency between weak and strong ISS is about $\nu_0 \sim 15$ GHz or higher. This implies that at 15 GHz, the sources are scintillating in the strong scattering regime (or close to the boundary between weak and strong scattering), as opposed to weak ISS as assumed above. Assuming $\nu_0 \sim 15$ GHz, we estimate from the fitting function that compact components of $\theta \sim 20$ to 100 μas will exhibit ISS of 3–13 per cent modulation indices at an observing frequency of 15 GHz, comparable to our observations. Assuming similar underlying source populations between the OVRO and MASIV Survey samples, the source size–frequency scaling would be more consistent with that expected for conical jets.

4.3 Interday variability of Galactic-plane blazars

Sources observed at low Galactic latitudes have been found to exhibit rapid variations at cm wavelengths (Taylor & Gregory 1983), attributed to refractive ISS (Rickett 1986). These include the extragalactic source CL4 (Keen et al. 1973; Margon, Downes & Gunn 1981), which has been observed to exhibit variability on a time-scale of weeks at 5 and 15 GHz (Webster & Ryle 1976). In fact, Seaquist & Gilmore (1982) report 15 GHz interday flux variations in CL4, likely ISS caused by enhanced scattering at the Cygnus Loop.

While our CGRaBS-selected sample does not include sources at Galactic latitudes $|b| < 10°$, the radio counterparts of two Fermi-detected Galactic plane blazars, 3EG J2016+3657 and 3EG J2027+3429, show clear visual evidence of interday variability in their 15 GHz light curves (Kara et al. 2012), and have also been monitored by OVRO since 2008. 3EG J2027+3429 (J2025+3343) even appears to exhibit an ESE (Kara et al. 2012; Pushkarev et al. 2013). Although these two sources are not a part of our sample, we examine their variability amplitudes here and compare them with that of our sample.

From the OVRO light curves, we derived $D(4\,\mathrm{d})$ for these two sources and obtain $m_{D(4\,\mathrm{d})}$ of 3 per cent and 5 per cent, respectively. Their $m_{D(4\,\mathrm{d})}/m_\sigma$ values are 1.72 for 3EG J2016+3657 and 2.76 for 3EG J2027+3429, so the latter would have been selected as an interday variable based on our selection criteria. From Fig. 4, we can clearly see that these two sources, shown as black squares, are among the most variable of the strong >1 Jy level sources.

At Galactic latitudes of $|b| < 3°$, these two sources are observed through a highly turbulent ISM and heavily scattered sightlines in the direction of the Cygnus OB1 association (Spangler & Cordes 1998), with I_α of 88.4 R and 29.5 R for 3EG J2016+3657 and 3EG J2027+3429, respectively. Their large 4-d variability amplitudes at 15 GHz further strenghten our argument that ISS is responsible for the interday variability of these two sources and the most variable blazars in our CGRaBS sample.

4.4 Intermittent scintillators

As mentioned in Section 4.2, of the 53 sources that are observed through sightlines of $I_\alpha \geq 10$ R, only 11 of them were selected as interday variables. One possible explanation for this is that the WHAM I_α measurements were obtained at an angular resolution of 1°, much larger than the typical tens to hundreds of micro-arcsecond source sizes of scintillating components in blazars. The high values of I_α may not be representative of the actual sightline towards the source.

The strength of ISS is not only dependent on the line-of-sight scattering strength, but also on the compactness of the source (Rickett 1990; Narayan 1992; Koay et al. 2018). The non-scintillating sources seen through strongly scattered sightlines may simply not be sufficiently compact to exhibit significant ISS.

Additionally, the most compact components in these weakly variable sources may also be transient and not persistent over the entire 10-yr observing span of the OVRO monitoring program. Our selection criteria for the interday variables is biased towards sources that exhibit persistent variability on these short time-scales over a significant portion of the full 10 yr observing span. For sources with intermittent ISS, the mean variability amplitudes that we measure over the full 10 yr will be suppressed by the low variability amplitudes during epochs when the source is not scintillating. Lovell et al. (2008) found that only 25 per cent of flat-spectrum extragalactic sources scintillate in either 3 or all 4 epochs of the 5 GHz MASIV Survey, i.e. are persistent scintillators. Interestingly, this fraction is consistent with the fraction (21 per cent) of interday variables in the sample of sources with high H α intensities ($I_\alpha \geq 10$ R).

The light curve of J0502+1338 (Fig. 1) illustrates the potential effect of ISS intermittency on the selection of variables (Jauncey et al. in press). When the source is in a low state (with low mean flux densities), the amplitude of interday variability is relatively low. When the flux density increases, possibly due to a flare, the interday variability increases in amplitude. This can be physically explained by the ejection of a compact, scintillating component during the flare. The ISS may persist until the compact component expands and dissipates. The line-of-sight H α intensity of J0502+1338 is 12.7 R, and it is one of the sources observed through the Orion–Eridanus superbubble (see Section 4.7 below). But its $m_{D(4\,\mathrm{d})}/m_\sigma$ of 1.4 is below our selection threshold of 2; it was thus not selected as a significant interday variable source due to the fact that it scintillates strongly during only half of the observing period.

Besides changes in intrinsic source compactness, inhomogeneities in the structure of the intervening scattering screen can also cause intermittent ISS (Kedziora-Chudczer 2006; Koay et al. 2011b; de Bruyn & Macquart 2015; Liu et al. 2015), again resulting in lower mean variability amplitudes measured over the entire OVRO observing span.

The fraction of sources that exhibit significant ISS at one time or another is thus likely to be larger than the fraction of the most significant interday variables we identified, when these intermittent scintillators are included. For example, there are 77 sources in our sample with $m_{D(4\,\mathrm{d})} \geq 1.5 m_\sigma$. Of these, 21 of them are observed through sightlines with $I_\alpha \geq 10$ R, constituting 40 per cent of the high I_α sample. On the other hand, only 5 per cent of the $I_\alpha < 10$ R sample exhibit these $>1.5 m_\sigma$ variations. This example not only demonstrates the robustness of our result regardless of the selection threshold for the most significant variables, but also that ISS is still present in sources whose variability amplitudes are less significant.

Finding and confirming more of these sources will enable us to examine if this intermittency is mainly due to changes in source structure or the intervening ISM. The former may cause an increase in IDV during flaring states in blazars, as seen in J0502+1338 (Fig. 1). Based on a visual inspection of all sources with $I_\alpha \geq 10$ R, other intermittent scintillator candidates include J0559−1817, J0619−1140, J0630−1323, J1617−1122, and J1619−1817. More

sophisticated methods are required to systematically search for such intermittent scintillation in the OVRO data. One possibility is to separate each light curve into multiple epochs, and to calculate $D(4\,\mathrm{d})$ in each epoch separately or only during the high flux density states of the sources. This is beyond the scope of this paper, and will be explored in follow-up studies.

4.5 Intrinsic variability versus ISS of individual sources

While the Galactic dependence of the variability amplitudes confirms at a statistical level the contribution of ISS to the 15 GHz interday variability of a significant fraction of the interday variables and our full sample of sources, we cannot ascertain the origin of the interday variability of an individual source based solely on observations at a single frequency.

For example, since a flare can also lead to fast-time-scale intrinsic variability due to the compactness of the new source component, the large flux density variations observed in J0502+1338 (Fig. 1) during its high state may also have an intrinsic origin. Of the nine interday variables that have line of sight $I_\alpha < 10\,\mathrm{R}$, six of them, notably J0721+7120 and J1135−0428, exhibit large flares on time-scales less than a year (Fig. C1), which may have skewed their 4-d variability amplitudes towards larger values. However, we argue that a component that is compact enough to exhibit intrinsic variability on interday to monthly time-scales must also be sufficiently compact enough to scintillate, if the line of sight is highly scattered (Koay et al. 2018), which is clearly the case for J0502+1338.

J0721+7120 (S5 0716+714) is in fact well-known as a highly variable source at radio, optical, X-ray, and gamma-ray wavelengths (e.g. Fuhrmann et al. 2008; Gupta et al. 2012). Intra and interday variability has been detected for this source at cm and mm wavelengths (Agudo et al. 2006; Gupta et al. 2012; Lee et al. 2016). Although the 5 GHz intraday variations appear to exhibit annual cycles (Liu et al. 2012, 2013), characteristic of ISS, the origin of the intraday variations observed between 10 and 15 GHz is still strongly debated (Jauncey et al. in press). This highlights the complexity in distinguishing between ISS and intrinsic variability in individual sources.

4.6 The candidate extreme scintillator J0616−1041

J0616−1041 (Fig. C1 in Appendix C) exhibits large 18 per cent flux density variations on a time-scale of 4 d. Such high 4-d variability amplitudes, the strongest in our entire sample of interday variables after excluding the problematic source J0259−0018 (Appendix B), are almost comparable to that exhibited by the so-called 'extreme scintillators', of which only a handful are known, including PKS0405−385 (Kedziora-Chudczer et al. 1997), J1819+3845 (Dennett-Thorpe & de Bruyn 2000), and PKS1257−326 (Bignall et al. 2003).

The large amplitude variations observed in J0616−1041 cannot be attributed to errors in flux density measurements alone, even though flux-independent errors, such as thermal noise, are more significant for a weaker source. For the flux measurement errors of $m_\sigma \sim 5.5$ per cent for J0616−1041, equivalent to $D_\sigma = 2m_\sigma^2 = 0.006$, assuming that the noise is white and independent of time lag, D_σ contributes additively to the measured $D(\tau)$ across all values of τ. This will increase the measured amplitude of flux density variations. However, even if we subtract $D_\sigma = 0.006$ from $D(4\,\mathrm{d}) = 6.32 \times 10^{-2}$ to account for the noise contribution, the resultant $m_{D(4\mathrm{d})}$ is still ~ 17 per cent. Furthermore, the m_σ of J0616−1041 is comparable to that of the other weak ∼0.2 Jy sources in our sample (Fig. 4). It is therefore unlikely that the m_σ of J0616−1041 is underestimated.

If the large amplitude interday variability of J0616−1041 is indeed due to ISS, the detection of 1 extreme scintillator in our sample of 1158 sources is statistically consistent with the non-detection of any new extreme scintillators in the MASIV Survey sample of ∼500 sources (Lovell et al. 2008).

Such extreme scintillation can occur if the source is ultracompact, or if there is an intervening, highly turbulent scattering screen located relatively close to the Earth. With a line of sight $I_\alpha = 18.94\,\mathrm{R}$, J0616−1041 appears to be observed through a heavily scattered sightline. Assuming that the transition frequency between weak and strong scintillation is $\nu_0 = 15\,\mathrm{GHz}$ at the line of sight towards this source, as given by Walker (2001), we estimate that to exhibit such high amplitude scintillation, the source must be about 16 μas in angular size for a scattering screen located at the typical distance of 500 pc from the Earth. At a mean flux density of ∼0.2 Jy, such a compact source would have an apparent brightness temperature of $\sim 10^{12}$ K. Assuming an equipartition brightness temperature of $\sim 10^{11}$ K (Readhead 1994; Lähteenmäki, Valtaoja & Wiik 1999), a Doppler boosting factor of ∼10 is required, well within the measured range of values for blazars (Hovatta et al. 2009). For a less stringent source compactness of 100 μas, the scattering screen has to be very close, of the order of ∼ 10 pc away from the Earth.

For the well-known extreme scintillators such as PKS1257−326 and J1819+3845, the high amplitude variations are attributed to the presence of nearby (<10 pc), highly turbulent scattering screens (Bignall et al. 2006; Macquart & de Bruyn 2007; de Bruyn & Macquart 2015; Vedantham, de Bruyn & Macquart 2017c), rather than to the compactness of the sources themselves. Due to the very nearby scattering screens, an important feature of these well-known extreme scintillators is their rapid intraday (and even intrahour) variability time-scales. For example, PKS1257−326 is known to vary in flux density by up to 40 per cent on a time-scale of 45 min (Bignall et al. 2003). Follow-up observations of J0616−1041 at a higher intraday cadence are required to confirm its status as a rapid scintillator in the mould of the well-known extreme, intrahour scintillators like PKS1257−326, as well as providing better constraints on the properties of the scattering screen. If the rapid variations are confirmed, metre-wave polarimetry can be used to 'image' the scattering cloud towards the source, as was done for J1819+3845 (Vedantham et al. 2017c), thus providing strong constraints on its distance and structure. There are, however, hints that the scattering screen of J0616−1041 may be a few hundred pc away from the Earth, which we discuss later in Section 4.7.1.

4.7 Clustering of interday variables through the Orion–Eridanus superbubble

Fig. 8 shows the distribution of the OVRO blazars on the sky in Galactic coordinates. The interday variables are shown as blue stars. The colour map shows the H α intensities from the WHAM Survey (Haffner et al. 2003), where we also include the data from the Southern sky survey (Haffner et al. 2010).

The sky distribution of the interday variables shows a clear dependence on the structures of the ionized gas in our Galaxy, strengthening the argument for their ISS-induced variability. In particular, more than half (11 of 20) of the interday variables are observed through the highly ionized region between longitudes of 175° and 240° and latitudes of −10° to −50°. This region is associated with the Orion–Eridanus superbubble, which contains gas with properties similar to that of the warm ionized medium

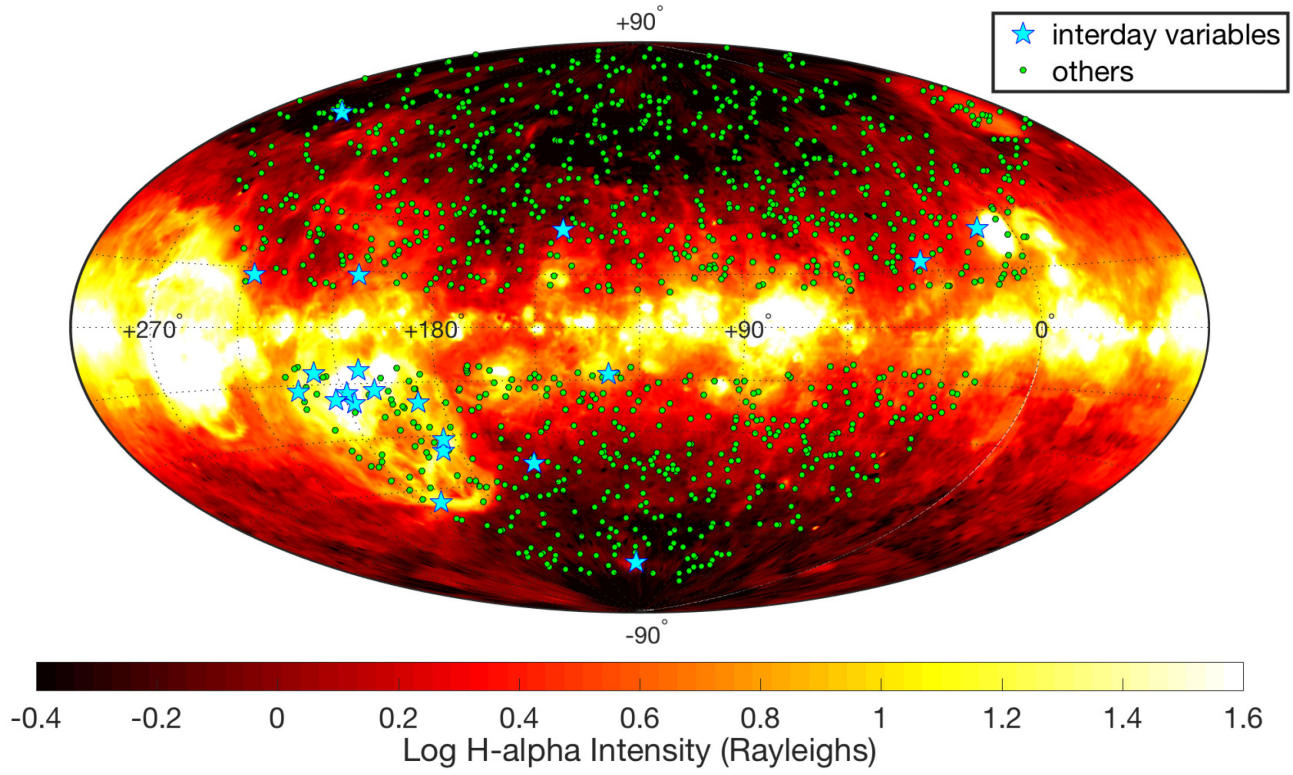

Figure 8. All-sky H α intensity map from the WHAM Survey (Haffner et al. 2003, 2010) shown in Galactic coordinates. The coordinates of the 1158 sources in the OVRO sample are shown as green circles or blue stars, where the latter represents the 20 sources that exhibit the most significant 4d variability amplitudes ($m_{D(4\,\mathrm{d})} \geq 2m_\sigma$, excluding J0259−0018).

(O'Dell et al. 2011), photoionized by the hot, giant stars of the Orion OB1 association (Brown, de Geus & de Zeeuw 1994; Brown, Hartmann & Burton 1995).

4.7.1 *Origin of extreme scintillation?*

Recently, the scattering structures responsible for the extreme scintillation of PKS1257−326 and J1819+3845 have been found to be associated with nearby hot stars Alhakim and Vega, respectively (Walker et al. 2017). They appear to be radially elongated filamentary structures pointing towards the host star, which Walker et al. (2017) suggest to be cometary 'tails' of molecular globules analogous to that observed in the Helix nebula. Interestingly, J0616−1041 is observed through the Orion–Eridanus superbubble. Perhaps the scattering screen of J0616−1041, as well as that of the other IDV sources observed through this region, may comprise similar anisotropic structures associated with the hot O and B stars in the region. If this is the case, the fact that these scattering structures are located at about 300–500 pc away from the Earth (Brown et al. 1995), suggests that J0616−1041 may indeed be ultracompact.

We note that J0616−1041 also happens to be the lowest flux density source among the 20 interday variables. If these compact blazars are brightness temperature-limited, either due to the inverse-Compton catastrophe (Kellermann & Pauliny-Toth 1969) or energy equipartition between the magnetic fields and electrons (Readhead 1994; Lähteenmäki et al. 1999), their angular sizes are expected to scale as $\theta \propto \sqrt{S_{15}}$. The weakest sources are also therefore most likely to be the most compact in angular size and thereby scintillate more strongly (Lovell et al. 2008; Koay et al. 2018).

4.7.2 *Implications for the high-energy neutrino source TXS 0506+056*

The blazar TXS 0506+056 (J0509+0541) was recently identified as a source of high-energy neutrinos (IceCube Collaboration 2018a,b). It is observed through the Orion–Eridanus superbubble, with $I_\alpha =$ 23.3 R. This source is in our sample, but its $m_{D(4\,\mathrm{d})}/m_\sigma$ of 1.7 means it narrowly also missed being classified as one of the interday variables. It is a well-known scintillator at lower frequencies (Lovell et al. 2008, Edwards et al. in preparation). The fact that this source is observed through this special region in our Galaxy means that any attempt to interpret its radio intra/interday variability (Tetarenko et al. 2017) in connection to that at other wavelengths, or to its intrinsic jet properties, will need to be carried out with caution.

5 SUMMARY AND CONCLUSIONS

In this study, we have characterized the 15 GHz variability amplitudes of 1158 radio-selected blazars monitored over ∼10 yr by the OVRO 40-m telescope, at the shortest observed time-scale of 4 d, to determine the origin of the interday flux density variations. Our main findings can be summarized as follows:

(i) The 4 to 20-d structure function amplitudes show a significant dependence on line-of-sight Galactic H α intensities, demonstrating the presence of ISS in the OVRO blazar light curves on time-scales of days and weeks.

(ii) Of the 1158 sources, we identified 20 that exhibit significant interday variability on 4-d time-scales. Based on the higher fraction (21 per cent) of these interday variables detected through sightlines with $I_\alpha \geq 10$ R compared to only 0.8 per cent detected through

weakly scattered sightlines of $I_\alpha < 10$ R, we argue that the 3–13 per cent flux density variations observed in these sources are mainly driven by ISS.

(iii) ISS is likely also present in the interday variations of a larger fraction of sources that exhibit less significant variability, i.e. $1.5 \lesssim m_{D(4\,\mathrm{d})}/m_\sigma < 2$. Our selection of significant variables missed out on intermittent scintillators such as J0502+1338 that are observed through heavily scattered sightlines, but exhibit significant ISS only during high flux density states; we interpret this as due to the ejection of new compact components that scintillate during a flare. Improved methods need to be developed to search for and identify such intermittent scintillators in these long-term data, to better understand the full population of scintillating sources at 15 GHz.

(iv) We have identified J0616−1041, displaying 18 per cent flux density variations on 4-d time-scales, as a candidate extreme scintillator. This source either contains an ultracompact core of the order of ∼10 μas, or is observed through a highly turbulent scattering screen located no more than 10 pc away from the Earth. Follow-up observations will enable us to confirm if this candidate is indeed scintillating rapidly on intraday time-scales.

(v) Of the 20 sources we classified as interday variables, more than half of them (11 sources, including J0616−1041), are observed through the Orion–Eridanus superbubble. This highly turbulent and ionized region appears to be an important region of interstellar scattering at 15 GHz. The high-energy neutrino source TXS 0506+056 is observed through this region, so its intra/interday radio variability will need to be interpreted with this in mind.

ISS is already known to dominate the intra and interday variability of compact, flat-spectrum radio sources up to 8 GHz. While ISS is typically ignored or assumed to be unimportant at 15 GHz, we have demonstrated through this work that ISS is still a significant contributor to intra and interday variability of compact sources at this frequency, especially through heavily scattered sightlines with high electron column densities, i.e. $I_\alpha \geq 10\,R$. These short term ISS-induced flux density variations are often superposed on larger amplitude intrinsic variations occurring on longer time-scales of $\gtrsim 100$ d.

In order to distinguish between ISS-induced and intrinsic inter/intraday variations of AGNs at 15 GHz and below, coeval monitoring at multiple frequencies, including at above 20–40 GHz, is required. Even then, opacity effects may smear out the rapid intrinsic variations at lower frequencies, making it difficult to search for cross-correlated variability in multifrequency light curves. Future surveys and monitoring of AGN radio variability will therefore need to be conducted at frequencies greater than 15 GHz if the goal is to study the intrinsic causes of intraday variability in radio AGNs, particularly if the sources are seen through thicker regions of the Galaxy. An alternative is to select sources only at higher Galactic latitudes where ISS at 15 GHz is less significant.

ACKNOWLEDGEMENTS

We thank the anonymous reviewer for the helpful suggestions to improve the manuscript. JYK thanks Keiichi Asada, Satoki Matsushita, Wen-Ping Lo, and Geoff Bower for helpful discussions. TH was supported by the Academy of Finland projects #317383 and #320085. WM and RR acknowledge support from CONICYT project Basal AFB-170002. This research has made use of data from the OVRO 40-m monitoring program (Richards et al. 2011) which is supported in part by the National Aeronautics and Space Administration (NASA) grants NNX08AW31G, NNX11A043G, and NNX14AQ89G and National Science Foundation (NSF) grants AST-0808050 and AST-1109911. The Wisconsin Hα Mapper and its Hα Sky Survey have been funded primarily by the NSF. The facility was designed and built with the help of the University of Wisconsin Graduate School, Physical Sciences Lab, and Space Astronomy Lab. National Optical Astronomy Observatory (NOAO) staff at Kitt Peak and Cerro Tololo provided on-site support for its remote operation.

REFERENCES

Agudo I. et al., 2006, A&A, 456, 117
Armstrong J. W., Rickett B. J., Spangler S. R., 1995, ApJ, 443, 209
Becker R. H., White R. L., Helfand D. J., 1995, ApJ, 450, 559
Bignall H. E. et al., 2003, ApJ, 585, 653
Bignall H. E., Macquart J.-P., Jauncey D. L., Lovell J. E. J., Tzioumis A. K., Kedziora-Chudczer L., 2006, ApJ, 652, 1050
Bignall H. E., Croft S., Hovatta T., Koay J. Y., Lazio J., Macquart J.-P., Reynolds C., 2015, Proc. Sci., Time domain studies of Active Galactic Nuclei with the Square Kilometre Array. SISSA, Trieste, PoS#58
Blandford R., Narayan R., Romani R. W., 1986, ApJ, 301, L53
Blandford R. D., Königl A., 1979, ApJ, 232, 34
Brown A. G. A., de Geus E. J., de Zeeuw P. T., 1994, A&A, 289, 101
Brown A. G. A., Hartmann D., Burton W. B., 1995, A&A, 300, 903
Coles W. A., Frehlich R. G., Rickett B. J., Codona J. L., 1987, ApJ, 315, 666
de Bruyn A. G., Macquart J.-P., 2015, A&A, 574, A125
Dennett-Thorpe J., de Bruyn A. G., 2000, ApJ, 529, L65
Duffett-Smith P. J., Readhead A. C. S., 1976, MNRAS, 174, 7
Fiedler R. L., Dennison B., Johnston K. J., Hewish A., 1987, Nature, 326, 675
Fuhrmann L. et al., 2008, A&A, 490, 1019
Goldreich P., Sridhar S., 1995, ApJ, 438, 763
Goodman J., Narayan R., 2006, ApJ, 636, 510
Gupta A. C. et al., 2012, MNRAS, 425, 1357
Haffner L. M., Reynolds R. J., Tufte S. L., Madsen G. J., Jaehnig K. P., Percival J. W., 2003, ApJS, 149, 405
Haffner L. M. et al., 2010, ASP Conf. Ser., 438, 388
Healey S. E. et al., 2008, ApJS, 175, 97
Heeschen D. S., Rickett B. J., 1987, AJ, 93, 589
Hovatta T., Valtaoja E., Tornikoski M., Lähteenmäki A., 2009, A&A, 494, 527
Hovatta T. et al., 2015, MNRAS, 448, 3121
IceCube Collaboration, 2018, Science, 361, eaat1378
IceCube Collaboration, 2018, Science, 361, 147
Jauncey D. L., Kedziora-Chudczer L., Lovell J. E. J., Nicolson G. D., Perley R. A., Reynolds J. E., Tzioumis A. K., Wieringa M. H., 2000, in Hirabayashi H., Edwards P. G., Murphy D. W., eds, Astrophysical Phenomena Revealed by Space VLBI, ISAS, Sagamihara, p. 147
Jauncey D. L. et al., Adv. Space Res., (in press)
Kara E. et al., 2012, ApJ, 746, 159
Kedziora-Chudczer L., 2006, MNRAS, 369, 449
Kedziora-Chudczer L., Jauncey D. L., Wieringa M. H., Walker M. A., Nicolson G. D., Reynolds J. E., Tzioumis A. K., 1997, ApJ, 490, L9
Keen N. J., Wilson W. E., Haslam C. G. T., Graham D. A., Thomasson P., 1973, A&A, 28, 197
Kellermann K. I., Pauliny-Toth I. I. K., 1969, ApJ, 155, L71
Koay J. Y. et al., 2011a, AJ, 142, 108
Koay J. Y., Bignall H. E., Macquart J.-P., Jauncey D. L., Rickett B. J., Lovell J. E. J., 2011b, A&A, 534, L1
Koay J. Y. et al., 2012, ApJ, 756, 29
Koay J. Y. et al., 2018, MNRAS, 474, 4396
Lähteenmäki A., Valtaoja E., Wiik K., 1999, ApJ, 511, 112
Lee J. W., Lee S.-S., Kang S., Byun D.-Y., Kim S. S., 2016, A&A, 592, L10
Liodakis I., Hovatta T., Huppenkothen D., Kiehlmann S., Max-Moerbeck W., Readhead A. C. S., 2018a, ApJ, 866, 137

Liodakis I., Romani R. W., Filippenko A. V., Kiehlmann S., Max-Moerbeck W., Readhead A. C. S., Zheng W., 2018b, MNRAS, 480, 5517
Liu X., Song H.-G., Marchili N., Liu B.-R., Liu J., Krichbaum T. P., Fuhrmann L., Zensus J. A., 2012, A&A, 543, A78
Liu X. et al., 2015, A&A, 578, A34
Liu B.-R., Liu X., Marchili N., Liu J., Mi L.-G., Krichbaum T. P., Fuhrmann L., Zensus J. A., 2013, A&A, 555, A134
Lovell J. E. J. et al., 2008, ApJ, 689, 108
Macquart J.-P., de Bruyn A. G., 2007, MNRAS, 380, L20
Margon B., Downes R. A., Gunn J. E., 1981, ApJ, 249, L1
Max-Moerbeck W. et al., 2014, MNRAS, 445, 428
Murphy T. et al., 2013, Publ. Astron. Soc. Aust., 30, e006
Narayan R., 1992, Philos. Trans. R. Soc., 341, 151
O'Dell C. R., Ferland G. J., Porter R. L., van Hoof P. A. M., 2011, ApJ, 733, 9
Pushkarev A. B. et al., 2013, A&A, 555, A80
Pushkarev A. B., Butuzova M. S., Kovalev Y. Y., Hovatta T., 2019, MNRAS, 482, 2336
Readhead A. C. S., 1994, ApJ, 426, 51
Richards J. L. et al., 2011, ApJS, 194, 29
Richards J. L., Hovatta T., Max-Moerbeck W., Pavlidou V., Pearson T. J., Readhead A. C. S., 2014, MNRAS, 438, 3058
Rickett B. J., 1986, ApJ, 307, 564
Rickett B. J., 1990, ARA&A, 28, 561
Rickett B. J., Lazio T. J. W., Ghigo F. D., 2006, ApJS, 165, 439
Savolainen T., Kovalev Y. Y., 2008, A&A, 489, L33
Seaquist E. R., Gilmore W. S., 1982, AJ, 87, 378
Spangler S. R., Cordes J. M., 1998, ApJ, 505, 766
Taylor A. R., Gregory P. C., 1983, AJ, 88, 1784
Tetarenko A. J., Sivakoff G. R., Kimball A. E., Miller-Jones J. C. A., 2017, Astron. Telegram, 10861, 1
Vedantham H. K. et al., 2017a, ApJ, 845, 90
Vedantham H. K. et al., 2017b, ApJ, 845, 89
Vedantham H. K., de Bruyn A. G., Macquart J.-P., 2017c, ApJ, 849, L3
Walker M. A., 1998, MNRAS, 294, 307
Walker M. A., 2001, MNRAS, 321, 176
Walker M. A., Tuntsov A. V., Bignall H., Reynolds C., Bannister K. W., Johnston S., Stevens J., Ravi V., 2017, ApJ, 843, 15
Webster A. S., Ryle M., 1976, MNRAS, 175, 95

APPENDIX A: ESTIMATION OF FLUX CALIBRATION UNCERTAINTIES

If we consider only $\sigma_{\rm err}$ (equation 3) in estimating the contribution of noise and instrumental effects (m_σ) to the interday variability amplitudes, such that $m_\sigma = {\rm median}(\sigma_{\rm err})/{\rm S}_{15}$, we find that this underestimates the m_σ of the strong sources. This can be seen in Figs A1 and A2, where the $m_{D(4\,{\rm d})}/m_\sigma$ peaks at a value higher than 1 for sources above 0.8 Jy. This suggests that the flux-dependent errors are underestimated. This can be attributed to errors in flux calibration that were not included during the estimation of $\sigma_{\rm err}$ in the OVRO data.

While a flux calibration error of 5 per cent is typically assumed based on the long-term variations observed in the flux calibrators, this is expected to be lower at interday time-scales. To constrain the 4-d flux calibration errors, we first obtained the 4-d structure function amplitudes of the flux calibrators 3C 286, and DR21. From equation (2), we derive their 4-d modulation indices, $m_{D(4\,{\rm d})}$, to be 1.5 per cent and 1.3 per cent, respectively. Since these are bright Jy level sources, the 4-d variability amplitudes will be dominated by flux-dependent errors, in addition to any intrinsic source variability that may introduce flux calibration errors to the science targets. These values of $m_{D(4\,{\rm d})}$ thus provide an upper limit on the the flux calibration errors.

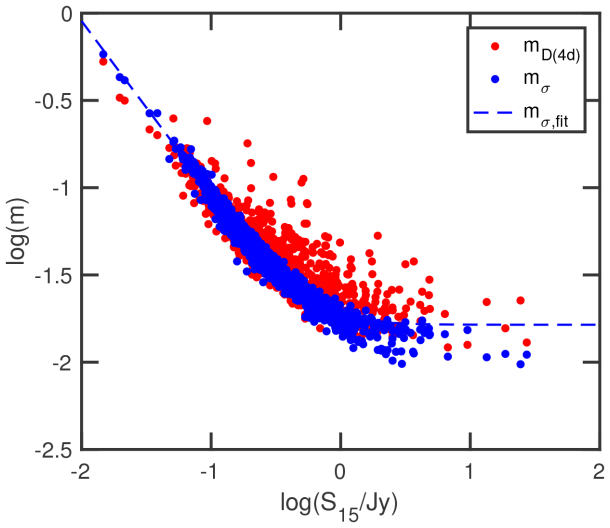

Figure A1. Modulation indices derived from the 4-d structure function amplitude, $m_{D(4\,{\rm d})}$, and $m_\sigma = {\rm median}(\sigma_{\rm err})/{\rm S}_{15}$, versus the 15 GHz flux density. Flux calibration errors are not included in the estimation of m_σ.

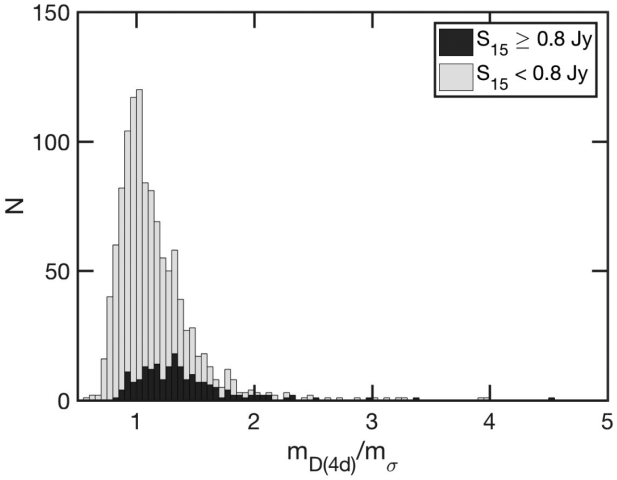

Figure A2. Histogram showing the distribution of the ratio of the 4-d variability amplitudes to the flux normalized measurement uncertainties of each source, $m_{D(4\,{\rm d})}/m_\sigma$, where $m_\sigma = {\rm median}(\sigma_{\rm err})/{\rm S}_{15}$. Since the flux calibration errors are not included in the estimation of m_σ, it can be seen that the uncertainties are underestimated for the strong sources with $S_{15} \geq 0.8$ Jy, for which the $m_{D(4\,{\rm d})}/m_\sigma$ distribution peaks at a value of about 1.3.

To estimate the flux calibration uncertainties, we let m_σ of each source be the flux normalized quadratic sum of $\sigma_{\rm err}$ of the source and the flux calibration error

$$m_\sigma = \frac{\sqrt{({\rm median}(\sigma_{\rm err}))^2 + (\sigma_{\rm cal})^2}}{S_{15}}, \quad \text{(A1)}$$

where the flux calibration error $\sigma_{\rm cal}$ is some fraction of the source flux density. Based on equation (A1), we determined that letting $\sigma_{\rm cal} \approx 1$ per cent of the source mean flux density is adequate to shift the peak of the $m_{D(4\,{\rm d})}/m_\sigma$ distribution of the strong sources to unity, as can be seen in Figs 4 and 5. This assumes that $m_{D(4\,{\rm d})}$ should be dominated by noise, instrumental, and systematic uncertainties as described in equation (4). This value of $\sigma_{\rm cal}$ is also consistent with the upper limits derived from the $m_{D(4\,{\rm d})}$ of the flux calibrators. We therefore adopt $\sigma_{\rm cal} = 0.01 S_{15}$ for this work, to correct for the

underestimation of m_σ in the strong sources. While we attribute this mainly to flux calibration errors, this term also folds in any residual flux-dependent errors that may be unaccounted for in the $\sigma_{\rm err}$ of the OVRO data.

APPENDIX B: ORIGIN OF LARGE INTERDAY FLUX VARIATIONS IN J0259−0018

J0259−0018 exhibits 24 per cent flux density variations on 4-d time-scales. Its light curve is shown in Fig. B1. It would have been remarkable if these large flux density variations are caused by ISS, as it would be comparable to that observed in a rare class of 'extreme scintillators', of which only a handful are known to date (Kedziora-Chudczer et al. 1997; Dennett-Thorpe & de Bruyn 2000; Bignall et al. 2003).

To confirm if the flux density variations observed in J0259−0018 have an astrophysical origin, we checked the light curves of four other sources located within ±5° of J0259−0018 on the sky. These sources are likely to share the same pointing source, and were observed at similar elevations and azimuths at the telescope. Our visual inspections find no correlated interday variability among these sources, so these variations are unlikely to be dominated by pointing or residual gain calibration errors. In any case, such errors are expected to dominate for stronger sources rather than weak ones like J0259−0018. Of these four nearby sources, two of them, J0305+0523 and J0318−0029, have comparable ∼0.1 Jy mean flux densities to J0259−0018. RFI characteristics are expected to be direction dependent, but would equally affect these two sources, so cannot explain the excess interday variability observed in J0259−001. The m_σ of J0305+0523 and J0318−0029 are also comparable to that of J0259−0018, but their $m_{D(4\,{\rm d})}$ are 2–4 factors lower than that of J0259−0018.

Finally, we checked the VLA Faint Images of the Radio Sky at Twenty-Centimeters (FIRST) Survey (Becker, White & Helfand 1995) catalogue to determine if confusion by a nearby bright source could be responsible for the large flux density variations. To our surprise, we found no source detected at the coordinates of RA = $02^{\rm h}59^{\rm m}28\overset{\rm s}{.}5100$ and Dec. = $-00^{\rm d}18'00\overset{''}{.}000$ as specified in the CGRaBS and OVRO catalogues for J0259−0018. On the other hand, there is a 0.2 Jy source located exactly 2 arcmin South. Checking the VLBA calibrator list, we found this source as J0259−0019, with coordinates of RA = $02^{\rm h}59^{\rm m}28\overset{\rm s}{.}5153$ and Dec. = $-00^{\rm d}19'59\overset{''}{.}968$. The flux density variations in the light curve of J0259−0018 could be caused by the source shifting around within the 2.6 arcmin primary beam at different hour angles.

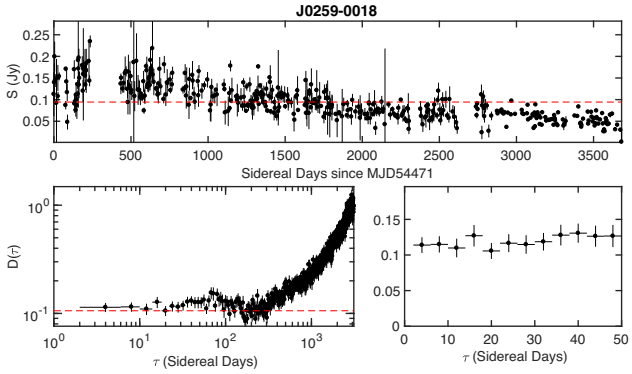

Figure B1. Top: Light curve for J0259−0018, where the horizontal dashed line denotes the mean flux density of the source. The error bars are given by equation (3) (Richards et al. 2011). Bottom: Structure function, $D(\tau)$, shown in its entirety in the left-hand panel, and for $\tau \leq 50$ d in the right-hand panel. The horizontal dashed line denotes D_{m15} (equation 2) derived from the intrinsic modulation indices estimated by Richards et al. (2014).

Unless its spectral index is highly inverted such that it is not detectable at 21 cm at the 0.121 mJy noise threshold of the FIRST Survey, which is highly unlikely, J0259−0018 probably does not exist, and in the original CGRaBS catalogue may in fact be a misidentification of J0259−0019. Even if J0259−0018 is detectable at 15 GHz, a source of comparable flux density located 2 arcmin away would still lead to confusion and increased flux density variations. We therefore rule out extreme scintillation in J0259−0018 and remove it from our list of significant interday variables.

APPENDIX C: LIGHT CURVES AND STRUCTURE FUNCTIONS OF SIGNIFICANT INTERDAY VARIABLES

In Fig. C1, we present the 15 GHz light curves measured by the OVRO 40-m telescope for the 20 sources which we detected to be significantly variable (see Section 4.2), together with their corresponding structure functions which we derived (Section 3.1). We exclude J0259−0018 due to problems described in Appendix B.

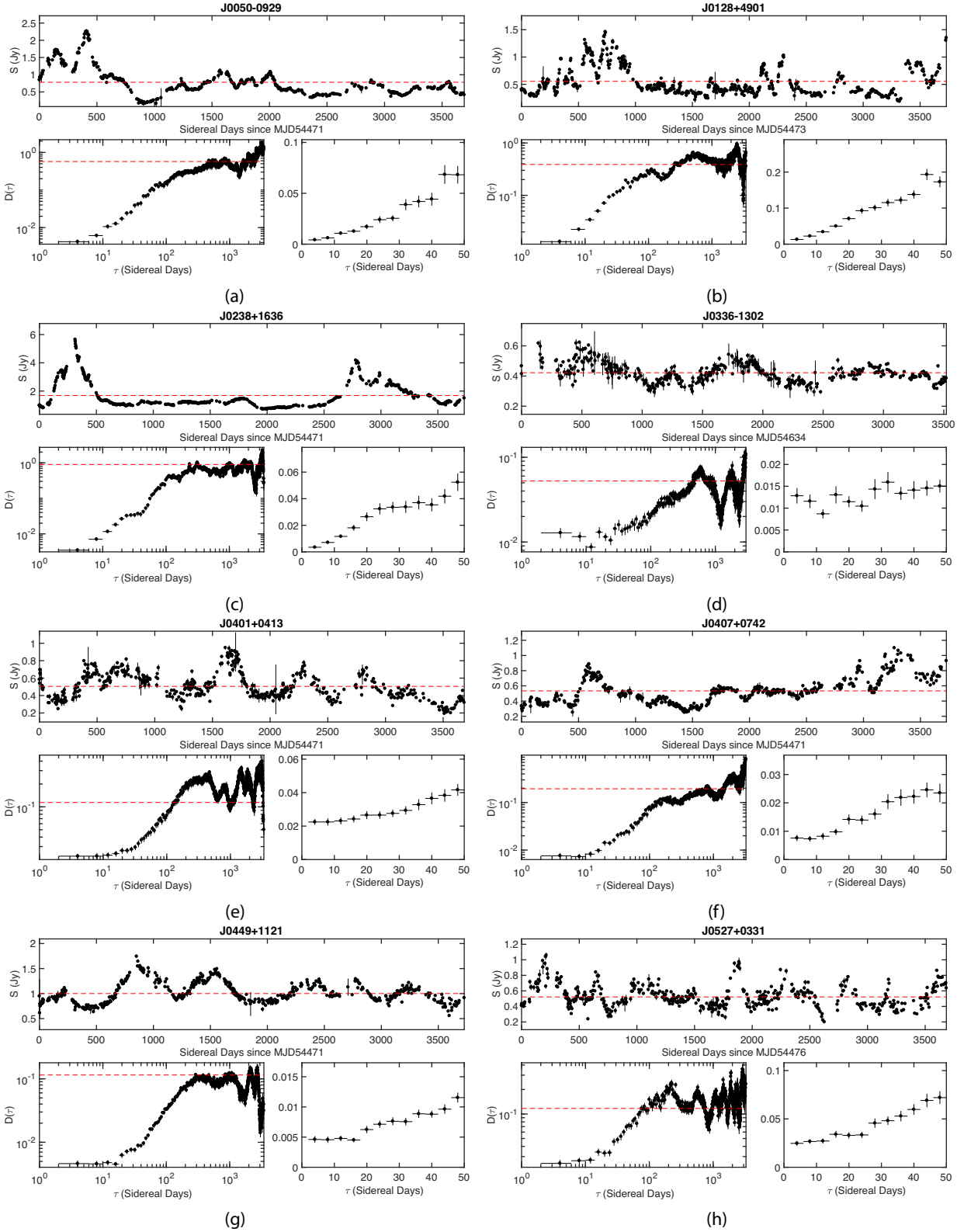

Figure C1. Light curves and structure functions of the 20 sources exhibiting significant variability amplitudes on 4-d time-scales, excluding J0259−0018. The light curves are shown in the top panel of each subfigure, where the horizontal dashed line denotes the mean flux density of the source. The error bars are given by equation (3) (Richards et al. 2011). The bottom panels of each subfigure show the structure function, $D(\tau)$, in its entirety in the left-hand panel, and for $\tau \leq 50$ d in the right-hand panel. The horizontal dashed line denotes D_{m15} (equation 2) derived from the intrinsic modulation indices estimated by Richards et al. (2014).

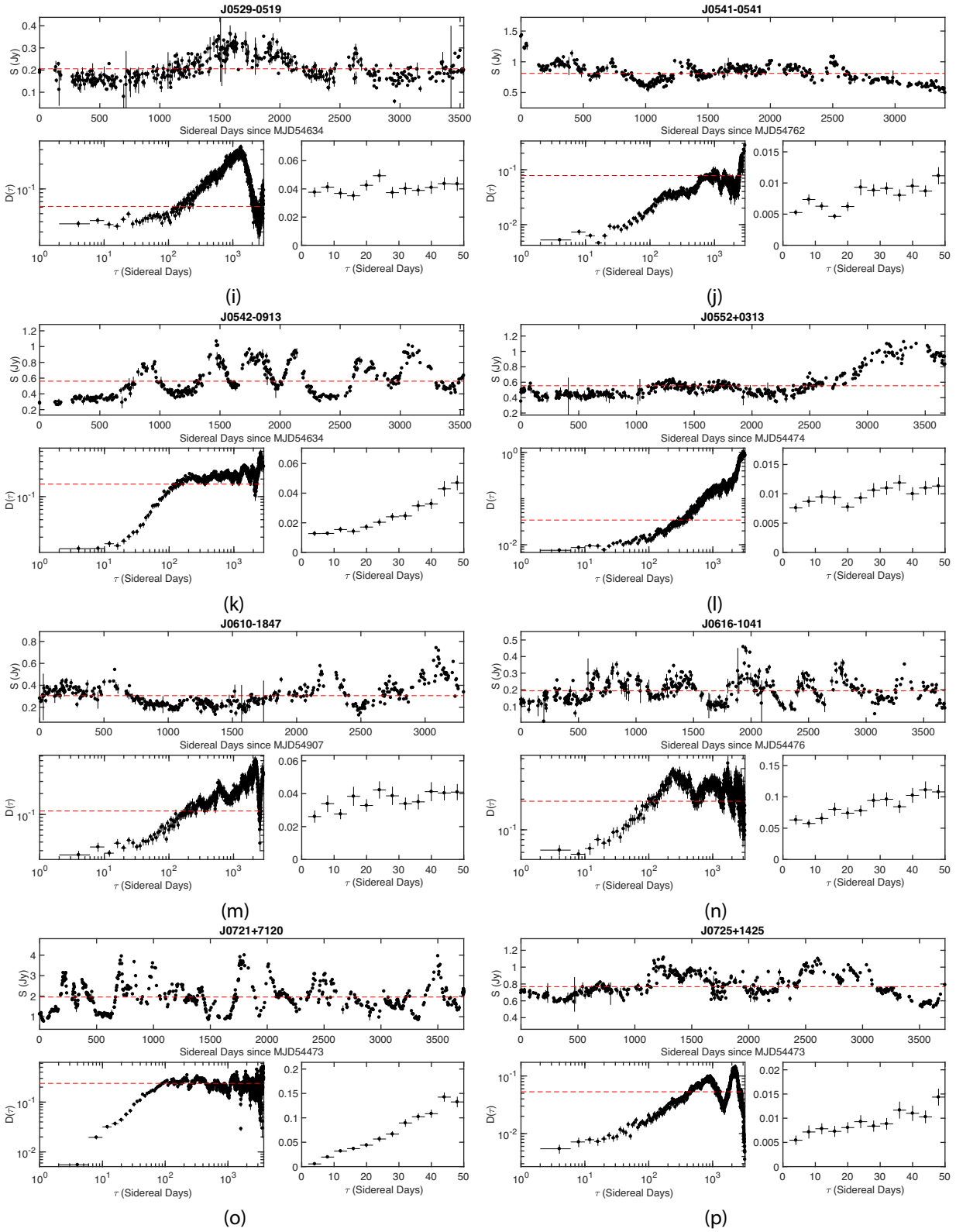

Figure C1. *continued.*

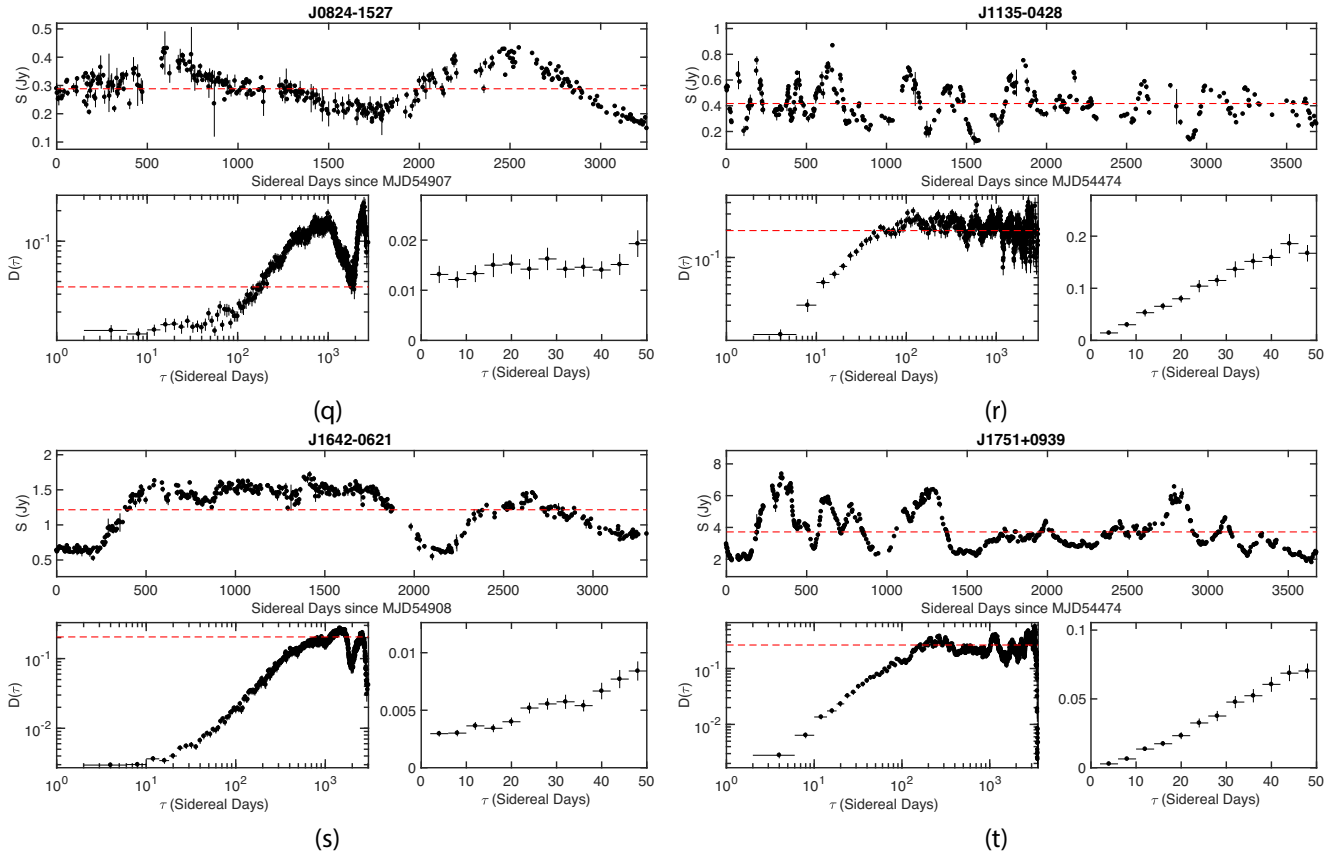

Figure C1. *continued.*

This paper has been typeset from a TEX/LATEX file prepared by the author.